# Structural, Biophysical, and Biochemical Elucidation of the SARS-CoV-2 Nonstructural Protein 3 Macro Domain

Meng-Hsuan Lin, San-Chi Chang, Yi-Chih Chiu, Bo-Chen Jiang, Tsung-Han Wu, and Chun-Hua Hsu*

ACCESS | Metrics & More | Article Recommendations | SI Supporting Information

**ABSTRACT:** The pandemic outbreak of a novel coronavirus, severe acute respiratory syndrome coronavirus 2 (SARS-CoV-2), has threatened the global public health and economy since late December 2019. SARS-CoV-2 encodes the conserved macro domain within nonstructural protein 3, which may reverse cellular ADP-ribosylation and potentially cut the signal of a viral infection in the cell. Herein, we report that the SARS-CoV-2 macro domain was examined as a poly-ADP-ribose (ADPR) binding module and possessed mono-ADPR cleavage enzyme activity. After confirming the ADPR binding ability via a biophysical approach, the X-ray crystal structure of the SARS-CoV-2 macro domain was determined and structurally compared with those of other viruses. This study provides structural, biophysical, and biochemical bases to further evaluate the role of the SARS-CoV-2 macro domain in the host response via ADP-ribose binding but also as a potential target for drug design against COVID-19.

**KEYWORDS:** SARS-CoV-2, macro domain, ADP-ribose, COVID-19, crystal structure
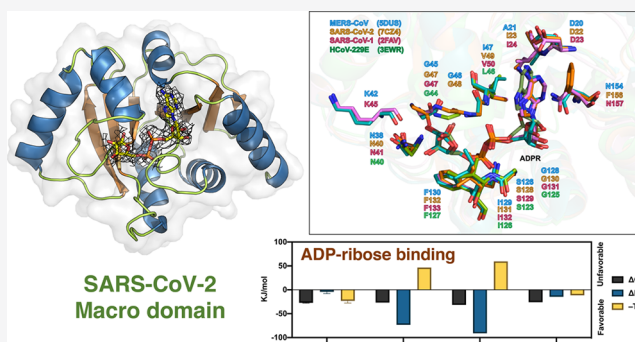
In late December 2019, patients with fever, respiratory symptoms, and severe pneumonia were reported in Wuhan, China. A novel virus, severe acute respiratory syndrome coronavirus 2 (SARS-CoV-2, also called 2019-nCoV), was identified as the causal pathogen. This newly emerged disease was named COVID-19. Then, after a few weeks, researchers declared a human-to-human transmission.[1−3] According to clinical observations related to the first German case, this disease seemed to cause many asymptomatic infections or slightly symptomatic infections.[4] Also, because of abundant travel at the very beginning of the outbreak during the lunar new year in China, COVID-19 soon spread to every province in China. With international air travel transmission, this disease was spread globally and rapidly.[5,6] According to the World Health Organization, as of September 14, 2020, there had been more than 28,918,900 cases, causing at least 922,252 deaths and the disease had spread globally.

The macro domain is a protein module ubiquitous in eukaryotes, bacteria, and archaea. The viral macro domain of SARS-CoV-1 was discovered in the past decade.[7] SARS-CoV-2 shares about 80% nucleotide identity with the original SARS-CoV-1 and harbors a macro domain in its nonstructural protein 3 (NSP3) located in the open reading frame 1ab (ORF1ab) (Figure 1). Macro domains were identified in several positive-strand RNA viruses, including coronaviruses and alphaviruses.

Virus macro domains were reported to have multiple functions, including a ADP-ribose (ADPR)[8−10] or poly-
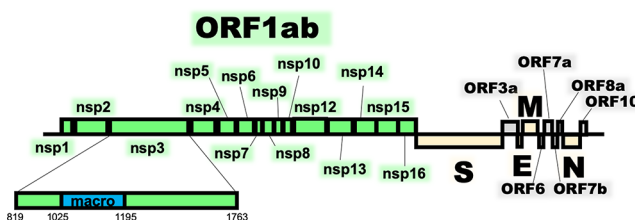


**Figure 1.** Genome of SARS-CoV-2. Structural and nonstructural proteins (nsps) in the SARS-CoV-2 genome. Genes of the macro domain in nsp3 are highlighted and in blue. Genes encoding structural proteins are in light yellow. The open reading frame (ORF) 1ab-harbored macro domain is in green. Other ORFs are in gray.

ADPR[9] interaction, adenine-rich RNA[11] binding, enzyme activities of ADPR-1″ phosphohydrolase,[7,9] and the removal of mono(ADP-ribose) from protein.[10] Accumulated evidence for virus macro domains pointed out a key relevance to host cellular ADP-ribosylation, which is a post-translational modification correlated with a wide spectrum of biological

phenomena, such as the innate immune response.[12,13] Moreover, mutation of macro domains of mouse hepatitis virus[14] and Sindbis virus[15] were reported to depress viral replication while disrupting ADPR binding ability. Also, the hepatitis E virus (HEV) macro domain could interact with HEV RNA methyltransferase[16] and ORF3[17] for involvement in both viral replication and release of the progeny virus.[18] Thus, a virus macro domain may play important roles in modulating host ADP-ribosylation.

In the present study, we characterized the basic protein properties and confirmed the biochemical function of PAR binding and deMARylation of the SARS-CoV-2 macro domain. Furthermore, we describe the crystal structure of the SARS-CoV-2 macro domain in complex with ADPR, with comparison to previously characterized macro domains of human CoVs. Hence, our study may be the essential groundwork for revealing the function of the SARS-CoV-2 macro domain in order to beat COVID-19.

## ■ RESULTS AND DISCUSSION

**ADPR Binding Ability of the SARS-CoV-2 Macro Domain.** The SARS-CoV-2 macro domain (pp1a residues 1025 to 1195) (Figure 1) was expressed and purified from *E. coli*. The final purified protein was a 171 amino acid protein (18 kDa) with four additional residues at the N-terminus resulting from the removal of the hexa-histidine tag after thrombin cleavage. Circular dichroism (CD) spectra revealed that the macro domain exhibited a stable $\alpha/\beta$ type folding pattern under various pH conditions but not below pH 4 (Figure 2A). To investigate the possible interaction of the
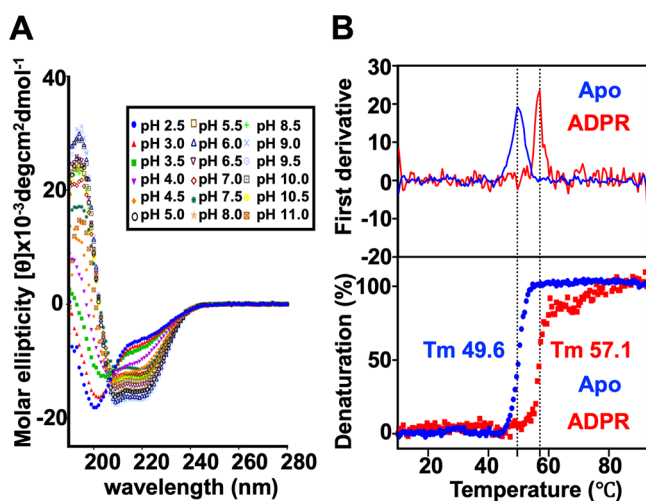


**Figure 2.** Circular dichroism (CD) spectra analysis of the SARS-CoV-2 macro domain. (A) CD spectra for the SARS-CoV-2 macro domain at various pH values (pH 2.5–11.0). (B) Thermal shift assay monitored by CD at 208 nm with or without ADPR. Signals with or without ADPR are in blue and red, respectively.

SARS-CoV-2 macro domain with ADPR, the thermal transition profiles of the protein with or without ADPR were monitored at 208 nm by using CD. Upon incubation of the SARS-CoV-2 macro domain with ADPR, the melting temperature ($T_m$) shifted significantly from 49.6 °C for the apo protein to 57.1 °C for the complex (Figure 2B). The significant increase in $T_m$ indicated the potent interaction between the SARS-CoV-2 macro domain and ADPR.

To examine the equilibrium dissociation constant ($K_d$) of the SARS-CoV-2 macro domain with ADPR, we used isothermal titration calorimetry (ITC) (Figure 3A). The ITC measurements confirmed ADPR binds to the SARS-CoV-2 macro domain at 1:1 stoichiometry with a dissociation constant ($K_d$) of 17.18 ± 6.03 $\mu$M. The mean enthalpy ($\Delta H$) was −4.28 ± 3.86 (kJ/mol) and entropy ($\Delta S$), 77.20 ± 15.69 (J/mol·K). The free energy value was −27.29 ± 0.86 (kJ/mol) (Table 1). The SARS-CoV-2 macro domain and HCoV-229E macro domain bound ADPR with a similar thermodynamic profile (favorable enthalpy and entropy) (Figure 3B, Table 1). Differential scanning fluorimetry (DSF) was used to examine the binding ability. After fitting DSF data, the $K_d$ was determined at 20.60 ± 7.7 $\mu$M (Figure 3C), which is similar to the calculated $K_d$ of 17.18 $\mu$M based on ITC data. Furthermore, nanoDSF analysis revealed that the addition of ADPR in the micromolar range significantly increased the melting point of the SARS-CoV-2 macro domain. In contrast, high concentrations of other nucleotides such as ADP or AMP were needed to the same extent of macro domain stabilization (Figure 3D).

**Enzyme Activity of De-mono-ADP-Ribosylation.** Like many positive-strand RNA viruses, SARS-CoV-2 contained a macro domain in its nonstructural protein 3 (NSP3) located at open reading frame 1ab (ORF1ab) (Figure 1). The viral macro domain may possess abilities to modulate viral replication and even suppress the host innate immune response by countering host antiviral ADP-ribosylation.[13] Besides, the de-mono-ADP-ribosylation (de-MAR) activity of viral macro domains was found to be critical for replication of pathogenic chikungunya virus, hepatitis E virus, and SARS-CoV-1.[10,19−21] Hence, a repeated measurement study ($n = 3$) investigating the de-MAR enzyme activity of the SARS-CoV-2 macro domain was examined. Varying concentrations of the SARS-CoV-2 macro domain (from 2.5 to 10 $\mu$M) were mixed with MARylated PARP10 CatD. The mono-ADP-ribosylation signals were decreased with increasing macro domain concentration, which indicates the de-MAR activity of the SARS-CoV-2 macro domain (Figure 4A,B).

**Poly-ADP-Ribose (PAR) Binding Ability.** Poly-ADP-ribosylation (PARylation) governs several fundamental processes of cell life and involves PAR covalently attaching onto a target protein via an ester-glycosidic bond. When triggered by a viral infection, PARylation acts as a stress signal to induce apoptosis and/or necrosis in the cell.[22] There is much evidence for the PAR binding ability of various viral macro domains.[9,23,24] Therefore, we confirmed the ability of the SARS-CoV-2 macro domain to interact with PAR by immuno-dot-blotting. The potential interactions with PAR were detected by the anti-PAR antibody. As expected, the SARS-CoV-2 macro domain showed PAR binding activity (Figure 4C). Recently, a preprint from Alhammad et al. showed that the SARS-CoV-2 macro domain did not bind PAR at the protein concentration of 60 pM by using immunoblotting.[25] We obtained a similar result that the SARS-CoV-2 macro domain did not show the interaction with PAR when the protein concentration was lower than 20 nM. However, we can observe the interaction of the SARS-CoV-2 macro domain and PAR in the conditions of 50 and 500 nM protein. The results indicate the PAR binding affinity of the SARS-CoV-2 macro domain may not be an event of strong binding.

**Overall Structure of the SARS-CoV-2 Macro Domain in Complex with ADPR.** For a comprehensive analysis of the
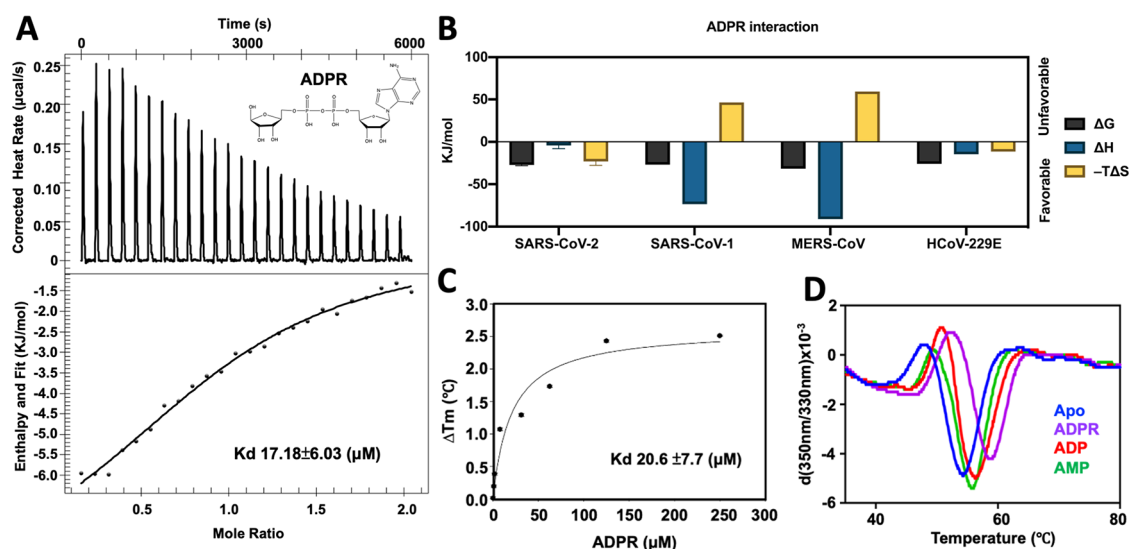
**Figure 3.** ADPR binding of the SARS-CoV-2 macro domain. (A) Isothermal titration calorimetry analysis of ADPR binding to the SARS-CoV-2 macro domain. Upper panel, raw data in $\mu$cal/s versus time showing heat release on titration of the 30-fold concentration of ADPR to the SARS-CoV-2 macro domain. Lower panel, integration of raw data yielding the heat per mole versus molar ratio. (B) Comparison of the thermodynamics of ADP-ribose binding by macro domains from SARS-CoV-2, SARS-CoV-1, MERS-CoV, and HCoV-229E. (C) DSF thermal shift detected by dye SYPRO Orange in the SARS-CoV-2 macro domain with increasing concentrations of ADPR. Data are the mean of 3 independent experiments. (D) DSF thermal shift assay of the protein intrinsic fluorescence from aromatic residues. The first deviation of signals from the protein apo form and with ADPR, ADP, and AMP are in blue, purple, red, and green, respectively.

**Table 1. Thermal-Dynamic Parameters for Binding of ADP-Ribose in Coronavirus (CoV) Macro Domains[a]**

| virus | macro domain | ligand | method | $K_d$ ($\mu$M) | $\Delta H$ (kJ/mol) | $\Delta S$ (J/mol·K) | $-T\Delta S$ (kJ/mol) | $\Delta G$ (kJ/mol) | references |
|---|---|---|---|---|---|---|---|---|---|
| SARS-CoV-2 | WT | ADPR | ITC | 17.18 | −4.28 | 77.00 | −23.00 | −26.74 | this study |
| | WT | ADPR | DSF | 20.60 | | | | | this study |
| | V24I/E25Q/F156N | ADPR | ITC | 2.32 | −0.48 | 106.53 | −31.75 | −32.22 | this study |
| MERS-CoV | WT | ADPR | ITC | 2.95 | −91.04 | −199.5 | 59.48 | −31.56 | 10 |
| | WT | ADPR | DSF | 3.12 | | | | | 10 |
| SARS-CoV-1 | WT | ADPR | ITC | 24 | −73.39 | −153.9 | 46.65 | −26.74 | 9 |
| HCoV-229E | WT | ADPR | ITC | 28.9 | −14.54 | 38.1 | −11.36 | −25.9 | 28 |

[a]SARS-CoV-2, severe acute respiratory syndrome coronavirus 2; MERS-CoV, Middle East respiratory syndrome coronavirus; SARS-CoV-1, severe acute respiratory syndrome coronavirus 1; HCoV-229E, human coronavirus 229E.

viral macro domain, we determined the crystal structure of the SARS-CoV-2 macro domain in complex with ADPR (Figure 5A). The crystals for diffraction data collection were grown more than 1 month (Figure S1A). The crystals belonged to space group $P4_1$ with unit cell parameters $a = b = 85.99$ Å, $c = 143.58$ Å, and $\alpha = \beta = \gamma = 90°$. In this crystal form, there were four molecules in the asymmetric unit with compact crystal packing (Figure S1B). The structure was refined at 3.83 Å resolution (PDB code: 7C33). During the revision of this Article, we obtained another crystal data set in the same condition after 4 months of growth. The crystal belonged to space group $P4_12_12$ with unit cell parameters $a = b = 84.74$ Å, $c = 143.24$ Å, and $\alpha = \beta = \gamma = 90°$. The second crystal structure was refined at 2.64 Å resolution (PDB code: 7CZ4) with R-factor and $R_{free}$ values of 17.08% and 21.47%, respectively. In this crystal data set, there were two protein molecules in an asymmetric unit (Figure S1C). Data collection and structure refinement statistics are in Table 2.

Further analytical gel filtration chromatography showed a single peak at the elution volume corresponding to the monomer molecular weight, confirming that the SARS-CoV-2 macro domain presented the monomeric state in solution (Figure S1D). The overall structure of the SARS-CoV-2 macro

domain consisted of six $\alpha$-helices and one seven-stranded $\beta$-sheet, the classical construction of macro domains (Figure 5B). The $\beta$-sheet is oriented at an order of $\beta1-\beta2-\beta7-\beta6-\beta3-\beta5-\beta4$ and sandwiched between $\alpha$-helices ($\alpha1$, $\alpha2$, and $\alpha3$ located at one side and $\alpha4$, $\alpha5$, and $\alpha6$, at the other side), so the SARS-CoV-2 macro domain showed a baseball glove-like structure and a groove between $\alpha$-helices formed the ligand-binding site. The $F_o - F_c$ difference map pointed out an actual ADPR that was bound in that ligand-binding site (Figure 5A).

The structural comparison with other viral macro domains by using the DALI server indicated that the SARS-CoV-2 macro domain was more similar to beta-CoVs (SARS-CoV-1, z-score of 32.6; Bat CoV-HKU4, z-score of 28.3; MERS-CoV, z-score of 24.0) than alpha-CoVs (feline CoV, z-score of 24.0; human CoV-229E, z-score of 23.9) (Figure 5C). $\beta2$, loop $\beta2-\alpha2$, and loop $\beta5-\alpha5$ were conserved among macro domains. Of note, the lower z-score (16.5) of MacroD1 (a human macro domain) indicated that there were many divergences between the human protein and viral macro domains, even with the same fold.

In the SARS-CoV-2 macro domain, the adenine moiety of ADPR was located in a cleft formed by loops $\beta1-\alpha1$, $\beta5-\alpha5$,
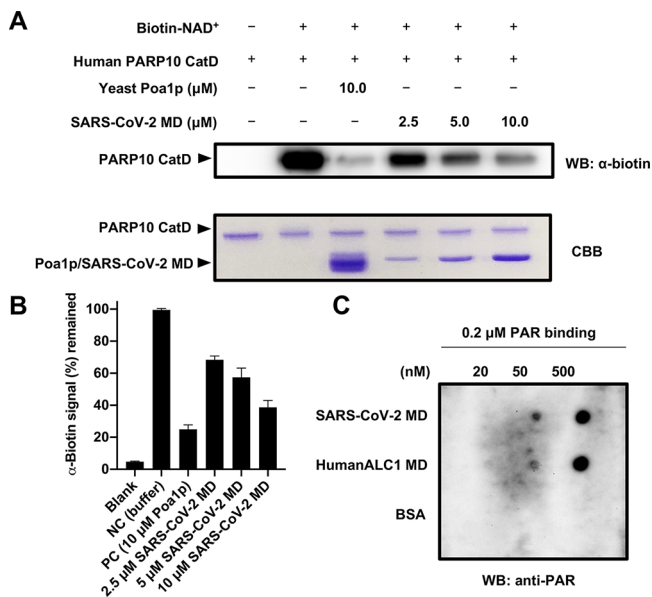
**Figure 4.** Functions of the SARS-CoV-2 macro domain. (A, B) Clarification of the de-MAR enzyme activity of the SARS-CoV-2 macro domain (MD). The auto-mono-ADP-ribosylated human PARP10 catalytic domain (CatD) was arranged by using biotin-NAD$^+$ as a substrate. Budding yeast macro domain Poa1p is a positive control. Varying concentrations of the SARS-CoV-2 macro domain (from 2.5 to 10 $\mu$M) were mixed with human PARP10 CatD and resolved by 15% acrylamide gel. Mono-ADP-ribosylation was detected by the Western blot assay with an anti-biotin antibody. The assays for de-MAR activity investigation are established three times. The relative densitometric bar graph of anti-biotin is presented (B). (C) SARS-CoV-2 macro domain PAR binding by the PAR overlay assay with increasing amounts of the domain as shown. The human ALC-1 macro domain (MD) was the positive control, and BSA was the negative control. The PARP1−PAR interaction by the PAR overlay assay with increasing amounts of recombinant PARP1. PAR binding was detected by dot-blotting with the anti-PAR antibody.

and $\beta6−\alpha6$ and the $\beta$-strand $\beta6$. The side-chain oxygen of D22 provided a hydrogen bond to connect the N-6 nitrogen of the pyrimidine group in the adenine moiety. Also, the adenine moiety of ADPR was hydrogen bonded via the N-1 nitrogen to the backbone amide proton of I23. Also, the adenine moiety resides in the hydrophobic cavity containing A21, I23, V49, P125, L126, A154, and F156. Furthermore, the stacking effects between the ring structures of P125, the adenine moiety, and F156 should stabilize the interaction with ADPR. Pyrophosphate groups and the distal ribose of ADPR lay in the crevice composed of loop $\beta2−\alpha2$ and loop $\beta4−\alpha4$. In the crack, the backbone amide nitrogen atoms of V49 and G130 and backbone amide nitrogen atoms of S128, G130, I131, and F132 interacted via hydrogen bonds with $\alpha$- and $\beta$-phosphate group oxygens, respectively. 1″ oxygen of the ADPR distal ribose and the nitrogen atom of the G48 backbone amide formed a hydrogen bond. The ribose-3″ oxygen atom formed a hydrogen bond with a nitrogen atom in the side chain of N40. The ribose-2″ oxygen atom arranged hydrogen bonds with the oxygen atom in the side chain of K44 and the nitrogen atom in the backbone amide of G46. The ribose-1″ oxygen atom formed a hydrogen bond with the nitrogen atom in the side chain of G46 (Figure 6A).

**Structural Comparison of Viral Macro Domains.**
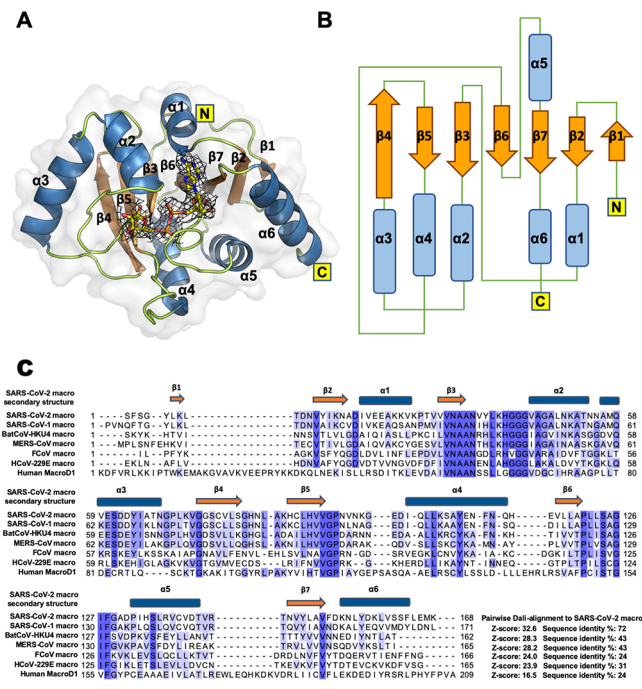During the progress of this study, the Center of Structural



**Figure 5.** Structure of the SARS-CoV-2 macro domain (7CZ4). (A) Overall structure. The surface of the SARS-CoV-2 macro domain is in light gray. Ligand ADPR is shown as a stick model covered by its electron density map. Blue, red, orange, and yellow represent nitrogen atoms, oxygens, phosphates, and carbons, respectively. (B) Topology diagram of the SARS-CoV-2 macro domain. (C) Structure-based alignment of viral macro domains and human macro domain (MacroD1). Conserved residues are in purple. Secondary structures of the SARS-CoV-2 macro domain, $\alpha$-helices and $\beta$-sheets, are in blue and orange, respectively, in (A)−(C).

Genomics of Infectious Diseases (CSGID) deposited the ADPR-bound SARS-CoV-2 macro domain determined by Michalska et al.[26] (PDB code: 6W02). Although the resolution of the structure (6W02, 1.50 Å) is higher, our two solved structures are almost identical with this one. The RMSD between the structures of 6W02 and 7C33 was 0.216 Å, while the RMSD between the structures of 6W02 and 7CZ4 was 0.242 Å. However, we noticed the loops surrounding the distal-ribose of ADPR show slight differences by comparing these three structural snapshots (Figure S1E). Recently, the apo form of the SARS-CoV-2 macro domain (6WEY) was reported by Frick et al.[27] They suggested that the conformational-changed region between the apo- and ADPR-bound form were located at loops $\beta3−\alpha2$, $\beta6−\alpha5$, and $\beta5−\alpha4$, which were also observed in the comparison of the apo form (6WEY) and our solved ADPR-bound form macro domain (7CZ4) (Figure S2A). Moreover, these conformational changes might reflect the entropy-driven ADPR binding defined by the ITC experiments (Figure 3B). In addition, we found that the surface electrostatic distributions were different between the apo- and ADPR-bound forms (Figure S2). Upon ADPR binding, the surface around the ligand-binding site became a positively charged cluster, which resulted from the movements of loops $\beta3−\alpha2$, $\beta6−\alpha5$, and $\beta5−\alpha4$ of the SARS-CoV-2 macro domain.

The solved crystal structure of the ADPR-complexed SARS-CoV-2 macro domain was structurally compared with other viral macro domains. The dissociation constant ($K_d$) of ADPR interacting with the MERS-CoV macro domain was 2.95 $\mu$M,[10]

D

**Table 2. Data Collection and Refinement Statistics of the SARS-CoV-2 Macro Domain in Complex with ADP-Ribose**

| PDB code | 7CZ4 | 7C33 |
|---|---|---|
| crystal parameters | | |
| space group | $P4_12_12$ | $P4_1$ |
| unit cell parameters | | |
| $a, b, c$ (Å) | 84.74; 84.74; 143.24 | 85.99; 85.99; 143.58 |
| $\alpha, \beta, \gamma$ (deg) | 90, 90, 90 | 90, 90, 90 |
| monomers per asymmetric unit cell | 2 | 4 |
| data collection | | |
| wavelength (Å) | 0.99984 | 0.99984 |
| resolution range (Å) | 29.32−2.64 (2.74−2.64) | 29.74−3.83 (3.97−3.83) |
| unique no. of reflections | 15963 | 9844 |
| total no. of reflections | 212632 | 34653 |
| $I/\sigma^{a,b}$ | 37.91 (3.18) | 7.68 (2.06) |
| $R_{merge}^{a,b}$ (%) | 10.7 (53.5) | 16.8 (58.4) |
| completeness$^a$ (%) | 90.52 (48.46) | 97.7 (91.7) |
| redundancy$^a$ | 13.3 (11.2) | 3.5 (2.5) |
| CC1/2 | 0.99 (0.98) | 0.90 (0.63) |
| refinement statistics | | |
| resolution (Å) | 2.64 | 3.83 |
| $R_{work}$ (%)/$R_{free}$ (%)$^c$ | 17.08/21.47 | 16.81/22.34 |
| RMSD | | |
| bonds (Å) | 0.008 | 0.010 |
| angles (o) | 0.97 | 1.02 |
| mean B-factor (Å²) | 41.23 | 26.76 |
| protein | 39.84 | 26.66 |
| ADP-ribose | 94.45 | 30.14 |
| Ramachandran plot (%) | | |
| favored | 97.29 | 98.47 |
| allowed | 2.71 | 1.53 |
| outliers | 0.0 | 0.0 |

$^a$Values in parentheses are for the highest resolution shell. $^b$$R_{merge} = \Sigma_h\Sigma_i|I_{h,i} - I_h|/\Sigma_h\Sigma_iI_{h,i}$, where $I_h$ is the mean intensity of the $i$ observations of the symmetry related reflections of $h$. $^c$$R_{work}/R_{free} = \Sigma|F_{obs} - F_{calc}|/\Sigma F_{obs}$, where $F_{calc}$ is the calculated protein structure factor from the atomic model ($R_{free}$ was calculated with 5% of the reflections selected).



**Figure 6.** Ligand binding site of virus macro domains. (A) SARS-CoV-2 macro domain ADPR binding site. Protein is presented as a cartoon illustration in light gray. Amino acids and ADPR are shown as sticks with oxygen in red, nitrogen in blue, and phosphorus in orange. Carbons of ADPR, residues generating hydrogen bonds to ligand, and residues interacting with ligands by hydrophobic interactions are colored in bright yellow, bright green, and wheat, respectively. Hydrogen bonds are black dashed lines. (B) Overlay of the ADPR-binding sites of the viral macro domains. Amino acids forming hydrogen bonds with ADPR are presented as sticks with oxygen in red and nitrogen in blue. Carbons of the residues from the macro domain of the MERS-CoV, SARS-CoV-2, SARS-CoV-1, and HCoV-229E are colored in light blue, orange, pink, and green, respectively. (C) Comparison between ADPR adenine groups with macro domains from MERS-CoV, SARS-CoV-2, and SARS-CoV-1. Blue represents a view inside the MERS-CoV macro domain. Yellow, SARS-CoV-2 macro domain. Pink, SARS-CoV-1 macro domain.

whereas that of ADPR binding with the SARS-CoV-2 macro domain was 15.41 μM, a little better than that for SARS-CoV-1, with $K_d$ 24 μM.[9] Also, the HCoV-229E macro domain interacted with ADPR with a $K_d$ of 28.9 μM[28] (Table 1). For further investigation of the structural differences between viral macro domains, we compared the ligand-binding site of macro domains from the SARS-CoV-2, SARS-CoV-1, MERS-CoV, and HCoV-229E (Figure 6B). A LigPlot$^+$ diagram[29] was used to illustrate these ligand-binding sites in detail (Figure S3).

Among these viral macro domains, the HCoV-229E macro domain had the weakest binding affinity. This may be due to the lack of hydrogen bonds, especially the one from conserved aspartate D19 located at loop β1−α1 to the adenine group of ADPR (Figures 6B and S3). While the interaction of ADPR and the macro domain from MERS-CoV or SARS-CoV-1 contains more hydrogen bonds, which may reflect the binding with favorable enthalpy defined by the ITC experiments (Figure 3B and Table 1). Macro domains of three beta-CoVs (MERS-CoV, SARS-CoV-1, and SARS-CoV-2), causing severe public health problems, bound to ADPR with different binding abilities. The macro domain from MERS-CoV presented the strongest binding affinity to ADPR. The ADPR binding ability
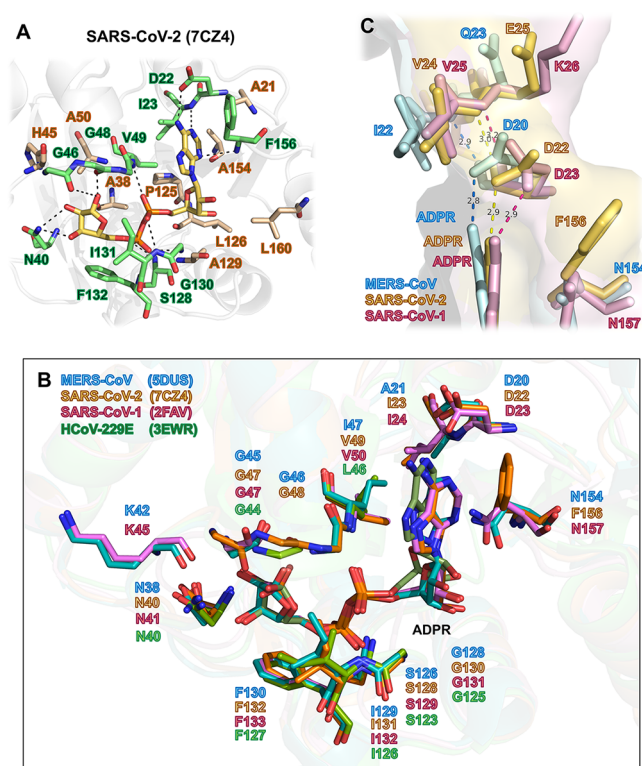
was better for the SARS-CoV-2 than the SARS-CoV-1 macro domain. This order was associated with the ADPR adenine group orientation (Figure 6C). In the MERS-CoV macro domain, the distance of the hydrogen bond between the N-6 nitrogen of the ADPR adenine group and the D20 side chain was 2.8 Å. The distance of the hydrogen bond connecting the backbones of the MERS-CoV macro domain I22 and D20 was 2.9 Å. Because of these critical connections between I22 and D20 in the MERS-CoV macro domain, the adenine moiety localized deep in the ligand-binding site. However, adenine groups complexed in SARS-CoV-2 and SARS-CoV-1 macro domains were at shallower positions inside the ligand-binding sites. In the SARS-CoV-2 macro domain, the N-6 nitrogen of the ADPR adenine group and D22 side chain formed a 2.9 Å hydrogen bond. The distance between the backbones of V24 and D22 was 3.0 Å. At the equivalent site of the SARS-CoV-1 macro domain, the V25 backbone contributed a linkage to D23 at a 3.2 Å distance. Moreover, the F156 residue located near the pyrimidine group of ADPR in the SARS-CoV-2 macro

domain. The ring-stacking effect was suspected to contribute to the orientation of ADPR in the SARS-CoV-2 macro domain.

It was likely a correlation between ADPR-binding ability and the N-6 nitrogen orientation at the adenine group of ADPR inside the ligand-binding site of the viral macro domain. The residues nearby the conserved residue D22, including V24, E25, and F156, may affect the orientation of the adenine group of ADPR. For better understanding, these three residues were mutated into I24, Q25, and N156 at the corresponding positions (Figure S4A) for mimicking the MERS-CoV macro domain, which possesses the higher ADPR binding affinity with $K_d \sim 2.95$ $\mu$M (Table 1). Then, the ADPR binding ability of the SARS-CoV-2 V24I/E25Q/F156N triple mutant was determined by ITC experiments. As expected, the result showed that ADPR binds to the V24I/E25Q/F156N triple mutant with a $K_d$ value of 2.32 ± 0.78 $\mu$M, which is presenting a higher affinity than wild-type (17.18 ± 6.03 $\mu$M) (Figure S4B).

## ■ CONCLUSION

While this work was in progress, the high-resolution crystal structures of the SARS-CoV-2 macro domain were released in the Protein Data Bank (PDB code: 6WEY and 6W02). The release of these high-resolution structures and remarks from our study can build confidence in understanding this macro domain from the novel virus SARS-CoV-2. Our study provides biochemical, biophysical, and structural knowledge of the SARS-CoV-2 macro domain. The SARS-CoV-2 macro domain may modulate human ADP-ribosylation by its de-MAR enzyme activity and PAR binding ability. The binding between the SARS-CoV-2 macro domain and ADPR was enthalpy and entropy driven. Moreover, D22 and the surrounding amino acids such as V24, E25, and F156 also optimized the orientation of ADPR. Our study provides a biochemical and biophysical basis for further investigating the role of the SARS-CoV-2 NSP3 macro domain in infections and supplies a structural landscape of this viral macro domain.

## ■ METHODS

**Protein Expression and Purification.** Production of the recombinant SARS-CoV-2 macro domain was similar to that for the MERS-CoV macro domain.[10] The DNA fragment of the SARS-CoV-2 macro domain was synthesized and cloned into the pET-28a (+) vector (Novagen) between the NdeI and XhoI sites. This resulting plasmid was then transformed into *E. coli* BL21 (DE3), which was grown at 37 °C and up to an $OD_{600}$ of 0.6. After inducing with 1 mM isopropyl-$\beta$-D-thiogalactoside (IPTG) and incubating overnight at 16 °C, *E. coli* cells were collected by centrifugation (6000 rpm, 10 min) and resuspended with lysis buffer (25 mM phosphate buffer, pH 7.0, 100 mM NaCl) followed by 20 min of sonication. Then, the supernatant was separated from the pellet by centrifugation at 13 000 rpm for 20 min at 4 °C. The recombinant SARS-CoV-2 macro domain with an N-terminal His-tag was purified with the Ni$^{2+}$-NTA column with an elution of 300 mM imidazole. The purified protein was dialyzed against lysis buffer with 0.5 mM dithiothreitol (DTT). The N-terminal His-tag was removed by thrombin cleavage at 10 °C overnight. The protein product with four additional residues (GSHM) at the N-terminus was further purified by gel filtration chromatography with the column Superdex 75 increased 16/60 (GE Healthcare). The purified protein was

stabilized in the gel-filtration buffer with 25 mM sodium phosphate and 100 mM NaCl at pH 7.0.

**Circular Dichroism (CD) Spectroscopy.** CD spectra were measured with 10 $\mu$M protein samples in 20 mM phosphate buffer, pH 2.5−11.0, placed into a 1 mm path-length cuvette and recorded on a Chirascan-plus qCD spectrometer. The thermal transition of protein samples with and without 1 mM ADPR was monitored at 208 nm from 10 to 95 °C at a scan rate of 1 °C/min. The melting temperature ($T_m$) was determined with the first derivative of the CD signal.

**Differential Scanning Fluorimetry (DSF).** The thermal shift assay with DSF involved the use of a StepOne Real-Time PCR Detection System (Thermo Fisher). A 25 $\mu$L mixture containing 2 $\mu$L of SYPRO Orange (Sigma-Aldrich), 10 $\mu$M protein sample, and various concentrations of ADPR was mixed in an 8-well PCR tube. Fluorescent signals were measured from 10 to 95 °C (excitation, 450−490 nm; detection, 560−580 nm). Data evaluation, $T_m$ determination, and data fitting for the dissociation constant ($K_d$) calculation involved the use of SigmaPlot.

**Label-Free Differential Scanning Fluorimetry (nanoDSF).** Label-free thermal shift assay experiments were performed with a Tycho NT.6 instrument (NanoTemper Technologies). A 10 $\mu$M protein sample and 30-fold concentration of ADPR, ADP, and AMP were mixed and heated in a glass capillary with temperature gradient from 35 to 95 °C at a rate of 30 K/min, and the internal fluorescence at 330 and 350 nm was recorded. Data analysis, data smoothing, and the calculation of derivatives involved using the internal evaluation features of the Tycho instrument. $T_m$ was determined by the first derivative of the signal (ratio of 350 nm/330 nm).

**Isothermal Titration Calorimetry (ITC).** The interactions with ADPR of the SARS-CoV-2 macro domain WT and V24I/E25Q/F156N were measured by ITC with a Nano ITC (TA Instruments). Aliquots of 4 $\mu$L of 3 mM ADPR were titrated by injection into 0.12 mM WT protein in 20 mM Tris-HCl buffer, pH 7.0, with 100 mM NaCl at 25 °C and 250 rpm of stirring. To measure the ADPR interaction of the SARS-CoV-2 macro domain V24I/E25Q/F156N triple mutant, aliquots of 4 $\mu$L of 1.2 mM ADPR were titrated by injection into 0.12 mM mutated protein in 20 mM Tris-HCl buffer, pH 7.0, with 100 mM NaCl at 25 °C and 250 rpm of stirring. Background heat from ligand to buffer titration was subtracted. The thermal parameters (enthalpy $\Delta H$ and entropy $\Delta S$), the stoichiometry of the binding ($n$), and the dissociation constant ($K_d$) were derived by fitting with an independent binding model with the use of Launch NanoAnalyze v2.3.6.

**DeMARylation Activity Assay.** For the DeMARylation activity assay, we used biotin-labeled ADP-ribosylated protein as substrate, like many other approaches for ADP-ribosylation-related assays.[30,31] To perform mono-ADP-ribosylation (MAR), a reaction mixture containing 10 $\mu$M hPARP10-CatD and 100 $\mu$M biotin-NAD$^+$ in 20 mM Tris-HCl, pH 8.0, 100 mM NaCl, and 0.5 mM DTT was incubated at a room temperature of 30 °C for 30 min. Varying concentrations of the SARS-CoV-2 macro domain (from 2.5 to 10 $\mu$M) were then added into the reaction; then, the samples were incubated at a room temperature of 30 °C for another 30 min. The reaction was terminated by adding 1% SDS, and proteins were resolved in 15% acrylamide gel. The gel was transferred onto a PVDF membrane (Bio-Rad) and probed with an anti-biotin polyclonal antibody (Bethyl Laboratories Inc.) (1/5000). The

budding yeast protein Poa1p was a positive control of de-MAR enzyme activity.[32] The de-MAR examinations were repeated three times.

**Poly ADPR (PAR) Binding Assay.** The PAR binding assay was modified from a previous study.[33] Recombinant proteins (i.e., SARS-CoV-2 macro domain, human ALC1 macro domain, and BSA), in amounts as indicated, were applied onto a nitrocellulose membrane (GE Healthcare). Then, the membrane was incubated overnight at 4 °C in TBST (20 mM Tris, pH 7.6, 100 mM NaCl, 0.05% Tween 20) containing 0.2 $\mu$M PAR. The next day, the membrane was washed with TBST containing 1 M NaCl for three times and, then, blocked in TBST supplemented with 5% (w/v) milk. Finally, the membrane was probed with an anti-PAR monoclonal antibody (Trevigen, catalog number: 4335-MC-100) (1/5000).

**Protein Crystallization and Data Collection.** The SARS-CoV-2 macro domain and ADPR were mixed in a molar ratio of 1:16. Protein crystallization trials were performed at 283 K by the sitting-drop vapor-diffusion method with commercial screening kits. Each crystallization drop was prepared with 1 $\mu$L of macro domain/ADPR at 14 mg/mL of mixing with an equal volume of mother liquor, and the mixture was equilibrated against a 100 $\mu$L reservoir solution. The crystals for data collection were grown at 283 K with a 37.5% precipitant mix (stock: 2.5% MPD, 25% PEG1000, 25% PEG3350), final concentration of 0.1 M, pH 8.5 buffer mix (stock: 1 M Tris, 1 M Bicine), and final concentration of 0.1 M carboxylic acids mix (stock: 0.2 M sodium formate, 0.2 M ammonium acetate, 0.2 M sodium citrate, 0.2 M sodium potassium, 0.2 M sodium oxamate). The crystal was cryoprotected in 4 M lithium formate and flash-cooled in liquid nitrogen at 100 K. The diffraction images were recorded in a 100 K nitrogen gas stream with the use of the TPS BL05A beamline (National Synchrotron Radiation Research Center, Taiwan) and processed by using HKL2000 software.[34,35] Four diffraction sets were merged to obtain the justifiable data quality for structural solving.

**Structural Determination.** The crystal structure of the ADPR-complex SARS-CoV-2 macro domain was determined by the molecular replacement method by using Phaser[36] in the PHENIX package.[37] The coordinates of the SARS-CoV-1 macro domain (PDB code: 2ACF)[7] served as a search model. The initial structure was refined with iterative cycles of simulated annealing, energy minimization, and manual rebuilding by using PHENIX refinement[37] and COOT.[38] Molecular visualizations were generated with PyMOL (The PyMOL Molecular Graphics System, Version 1.7, Schrödinger, LLC). Data collection and refinement statistics are summarized in Table 2.

## ■ ASSOCIATED CONTENT

### ⑤ Supporting Information

The Supporting Information is available free of charge at https://pubs.acs.org/doi/10.1021/acsinfecdis.0c00441.

> Figure S1, events during crystallization to obtain the ADPR complexed SARS-CoV-2 macro domain; Figure S2, structural comparison between the apo form and ADPR-bound form of the SARS-CoV-2 macro domain; Figure S3, interactions between viral macro domains and ADPR; Figure S4, MERS-CoV macro domain-mimics mutagenesis introduced into the SARS-CoV-2 macro domain (PDF)

### Accession Codes

The atomic coordinates and structure factors for the SARS-CoV-2 macro domain in complex with ADP-ribose (codes 7C33 and 7CZ4) have been deposited in the Protein Data Bank (http://wwpdb.org/).

## ■ AUTHOR INFORMATION

### Corresponding Author

**Chun-Hua Hsu** − *Genome and Systems Biology Degree Program, National Taiwan University and Academia Sinica, Taipei 10617, Taiwan; Department of Agricultural Chemistry and Institute of Biochemical Sciences, National Taiwan University, Taipei 10617, Taiwan;* ⓘ orcid.org/0000-0002-0008-7383; Phone: +886-2-33664468; Email: andyhsu@ntu.edu.tw

### Authors

**Meng-Hsuan Lin** − *Genome and Systems Biology Degree Program, National Taiwan University and Academia Sinica, Taipei 10617, Taiwan*

**San-Chi Chang** − *Department of Agricultural Chemistry, National Taiwan University, Taipei 10617, Taiwan*

**Yi-Chih Chiu** − *Genome and Systems Biology Degree Program, National Taiwan University and Academia Sinica, Taipei 10617, Taiwan*

**Bo-Chen Jiang** − *Department of Agricultural Chemistry, National Taiwan University, Taipei 10617, Taiwan*

**Tsung-Han Wu** − *Genome and Systems Biology Degree Program, National Taiwan University and Academia Sinica, Taipei 10617, Taiwan*

Complete contact information is available at:
https://pubs.acs.org/10.1021/acsinfecdis.0c00441

### Author Contributions

C.-H.H. conceived the study. M.-H.L., S.-C.C., and B.-C.J. performed the purification of the enzyme. Y.-C.C. performed the biochemical assays. M.-H.L. and S.-C.C. performed DSF, ITC, and crystallization. M.-H.L. and T.-H.W. performed the CD assay. M.-H.L. collected X-ray data. M.-H.L. and C.-H.H. determined and analyzed the crystal structure. M.-H.L. and C.-H.H. contributed to writing the manuscript. All authors reviewed the results and approved the final version of the manuscript.

### Notes

The authors declare no competing financial interest.

## ■ ACKNOWLEDGMENTS

# ■ REFERENCES

(1) Ralph, R., Lew, J., Zeng, T., Francis, M., Xue, B., Roux, M., Toloue Ostadgavahi, A., Rubino, S., Dawe, N. J., Al-Ahdal, M. N., Kelvin, D. J., Richardson, C. D., Kindrachuk, J., Falzarano, D., and Kelvin, A. A. (2020) 2019-nCoV (Wuhan virus), a novel Coronavirus: human-to-human transmission, travel-related cases, and vaccine readiness. *J. Infect. Dev. Countries* 14, 3−17.

(2) Shanmugaraj, B., Malla, A., and Phoolcharoen, W. (2020) Emergence of Novel Coronavirus 2019-nCoV: Need for Rapid Vaccine and Biologics Development. *Pathogens* 9, 148.

(3) Yu, P., Zhu, J., Zhang, Z., Han, Y., and Huang, L. (2020) A familial cluster of infection associated with the 2019 novel coronavirus indicating potential person-to-person transmission during the incubation period. *J. Infect. Dis.* 221, 1757−1761.

(4) Rothe, C., Schunk, M., Sothmann, P., Bretzel, G., Froeschl, G., Wallrauch, C., Zimmer, T., Thiel, V., Janke, C., Guggemos, W., Seilmaier, M., Drosten, C., Vollmar, P., Zwirglmaier, K., Zange, S., Wolfel, R., and Hoelscher, M. (2020) Transmission of 2019-nCoV Infection from an Asymptomatic Contact in Germany. *N. Engl. J. Med.* 382, 970−971.

(5) Hanscheid, T., Valadas, E., and Grobusch, M. P. (2020) Coronavirus 2019-nCoV: Is the genie already out of the bottle? *Travel Med. Infect Dis* 35, 101577.

(6) Rodriguez-Morales, A. J., MacGregor, K., Kanagarajah, S., Patel, D., and Schlagenhauf, P. (2020) Going global - Travel and the 2019 novel coronavirus. *Travel Med. Infect Dis* 33, 101578.

(7) Saikatendu, K. S., Joseph, J. S., Subramanian, V., Clayton, T., Griffith, M., Moy, K., Velasquez, J., Neuman, B. W., Buchmeier, M. J., Stevens, R. C., and Kuhn, P. (2005) Structural basis of severe acute respiratory syndrome coronavirus ADP-ribose-1″-phosphate dephosphorylation by a conserved domain of nsP3. *Structure* 13, 1665−1675.

(8) Makrynitsa, G. I., Ntonti, D., Marousis, K. D., Birkou, M., Matsoukas, M. T., Asami, S., Bentrop, D., Papageorgiou, N., Canard, B., Coutard, B., and Spyroulias, G. A. (2019) Conformational plasticity of the VEEV macro domain is important for binding of ADP-ribose. *J. Struct. Biol.* 206, 119−127.

(9) Egloff, M. P., Malet, H., Putics, A., Heinonen, M., Dutartre, H., Frangeul, A., Gruez, A., Campanacci, V., Cambillau, C., Ziebuhr, J., Ahola, T., and Canard, B. (2006) Structural and functional basis for ADP-ribose and poly(ADP-ribose) binding by viral macro domains. *J. Virol.* 80, 8493−8502.

(10) Cho, C. C., Lin, M. H., Chuang, C. Y., and Hsu, C. H. (2016) Macro Domain from Middle East Respiratory Syndrome Coronavirus (MERS-CoV) Is an Efficient ADP-ribose Binding Module: CRYSTAL STRUCTURE AND BIOCHEMICAL STUDIES. *J. Biol. Chem.* 291, 4894−4902.

(11) Tsika, A. C., Melekis, E., Tsatsouli, S. A., Papageorgiou, N., Mate, M. J., Canard, B., Coutard, B., Bentrop, D., and Spyroulias, G. A. (2019) Deciphering the Nucleotide and RNA Binding Selectivity of the Mayaro Virus Macro Domain. *J. Mol. Biol.* 431, 2283−2297.

(12) Fehr, A. R., Singh, S. A., Kerr, C. M., Mukai, S., Higashi, H., and Aikawa, M. (2020) The impact of PARPs and ADP-ribosylation on inflammation and host-pathogen interactions. *Genes Dev.* 34, 341−359.

(13) Alhammad, Y. M. O., and Fehr, A. R. (2020) The Viral Macrodomain Counters Host Antiviral ADP-Ribosylation. *Viruses* 12, 384.

(14) Eriksson, K. K., Cervantes-Barragan, L., Ludewig, B., and Thiel, V. (2008) Mouse hepatitis virus liver pathology is dependent on ADP-ribose-1″-phosphatase, a viral function conserved in the alpha-like supergroup. *J. Virol.* 82, 12325−12334.

(15) Park, E., and Griffin, D. E. (2009) The nsP3 macro domain is important for Sindbis virus replication in neurons and neurovirulence in mice. *Virology* 388, 305−314.

(16) Magden, J., Takeda, N., Li, T., Auvinen, P., Ahola, T., Miyamura, T., Merits, A., and Kaariainen, L. (2001) Virus-specific mRNA capping enzyme encoded by hepatitis E virus. *J. Virol.* 75, 6249−6255.

(17) Ding, Q., Heller, B., Capuccino, J. M., Song, B., Nimgaonkar, I., Hrebikova, G., Contreras, J. E., and Ploss, A. (2017) Hepatitis E virus ORF3 is a functional ion channel required for release of infectious particles. *Proc. Natl. Acad. Sci. U. S. A.* 114, 1147−1152.

(18) Anang, S., Subramani, C., Nair, V. P., Kaul, S., Kaushik, N., Sharma, C., Tiwari, A., Ranjith-Kumar, C. T., and Surjit, M. (2016) Identification of critical residues in Hepatitis E virus macro domain involved in its interaction with viral methyltransferase and ORF3 proteins. *Sci. Rep.* 6, 25133.

(19) Abraham, R., Hauer, D., McPherson, R. L., Utt, A., Kirby, I. T., Cohen, M. S., Merits, A., Leung, A. K. L., and Griffin, D. E. (2018) ADP-ribosyl-binding and hydrolase activities of the alphavirus nsP3 macrodomain are critical for initiation of virus replication. *Proc. Natl. Acad. Sci. U. S. A.* 115, E10457−E10466.

(20) Eckei, L., Krieg, S., Butepage, M., Lehmann, A., Gross, A., Lippok, B., Grimm, A. R., Kummerer, B. M., Rossetti, G., Luscher, B., and Verheugd, P. (2017) The conserved macrodomains of the non-structural proteins of Chikungunya virus and other pathogenic positive strand RNA viruses function as mono-ADP-ribosylhydrolases. *Sci. Rep.* 7, 41746.

(21) Fehr, A. R., Channappanavar, R., Jankevicius, G., Fett, C., Zhao, J., Athmer, J., Meyerholz, D. K., Ahel, I., and Perlman, S. (2016) The Conserved Coronavirus Macrodomain Promotes Virulence and Suppresses the Innate Immune Response during Severe Acute Respiratory Syndrome Coronavirus Infection. *mBio* 7, e01721−16.

(22) Hay, S., and Kannourakis, G. (2002) A time to kill: viral manipulation of the cell death program. *J. Gen. Virol.* 83, 1547−1564.

(23) Neuvonen, M., and Ahola, T. (2009) Differential activities of cellular and viral macro domain proteins in binding of ADP-ribose metabolites. *J. Mol. Biol.* 385, 212−225.

(24) Karras, G. I., Kustatscher, G., Buhecha, H. R., Allen, M. D., Pugieux, C., Sait, F., Bycroft, M., and Ladurner, A. G. (2005) The macro domain is an ADP-ribose binding module. *EMBO J.* 24, 1911−1920.

(25) Alhammad, Y. M. O., Kashipathy, M. M., Roy, A., Johnson, D. K., McDonald, P., Battaile, K. P., Gao, P., Lovell, S., and Fehr, A. R. (2020) The SARS-CoV-2 conserved macrodomain is a highly efficient ADP-ribosylhydrolase enzyme. *bioRxiv*, DOI: 10.1101/2020.05.11.089375.

(26) Michalska, K., Kim, Y., Jedrzejczak, R., Maltseva, N. I., Stols, L., Endres, M., and Joachimiak, A. (2020) Crystal structures of SARS-CoV-2 ADP-ribose phosphatase: from the apo form to ligand complexes. *IUCrJ* 7, 814−824.

(27) Frick, D. N., Virdi, R. S., Vuksanovic, N., Dahal, N., and Silvaggi, N. R. (2020) Molecular Basis for ADP-Ribose Binding to the Mac1 Domain of SARS-CoV-2 nsp3. *Biochemistry* 59, 2608−2615.

(28) Piotrowski, Y., Hansen, G., Boomaars-van der Zanden, A. L., Snijder, E. J., Gorbalenya, A. E., and Hilgenfeld, R. (2009) Crystal structures of the X-domains of a Group-1 and a Group-3 coronavirus reveal that ADP-ribose-binding may not be a conserved property. *Protein Sci.* 18, 6−16.

(29) Laskowski, R. A., and Swindells, M. B. (2011) LigPlot+: multiple ligand-protein interaction diagrams for drug discovery. *J. Chem. Inf. Model.* 51, 2778−2286.

(30) Vivelo, C. A., and Leung, A. K. (2015) Proteomics approaches to identify mono-(ADP-ribosyl)ated and poly(ADP-ribosyl)ated proteins. *Proteomics* 15 (2−3), 203−17.

(31) Loseva, O., Jemth, A. S., Bryant, H. E., Schuler, H., Lehtio, L., Karlberg, T., and Helleday, T. (2010) PARP-3 is a mono-ADP-ribosylase that activates PARP-1 in the absence of DNA. *J. Biol. Chem.* 285, 8054−8060.

(32) Jankevicius, G., Hassler, M., Golia, B., Rybin, V., Zacharias, M., Timinszky, G., and Ladurner, A. G. (2013) A family of macrodomain proteins reverses cellular mono-ADP-ribosylation. *Nat. Struct. Mol. Biol.* 20, 508−514.

(33) Popp, O., Veith, S., Fahrer, J., Bohr, V. A., Burkle, A., and Mangerich, A. (2013) Site-specific noncovalent interaction of the biopolymer poly(ADP-ribose) with the Werner syndrome protein regulates protein functions. *ACS Chem. Biol.* 8 (1), 179−88.

(34) Otwinowski, Z., and Minor, W. (1997) Processing of X-ray diffraction data collected in oscillation mode. *Methods Enzymol. 276,* 307−326.

(35) Aravind, L., Zhang, D., de Souza, R. F., Anand, S., and Iyer, L. M. (2014) The natural history of ADP-ribosyltransferases and the ADP-ribosylation system. *Curr. Top. Microbiol. Immunol. 384,* 3−32.

(36) Bunkoczi, G., Echols, N., McCoy, A. J., Oeffner, R. D., Adams, P. D., and Read, R. J. (2013) Phaser.MRage: automated molecular replacement. *Acta Crystallogr., Sect. D: Biol. Crystallogr. 69,* 2276−2286.

(37) Adams, P. D., Afonine, P. V., Bunkoczi, G., Chen, V. B., Davis, I. W., Echols, N., Headd, J. J., Hung, L. W., Kapral, G. J., Grosse-Kunstleve, R. W., McCoy, A. J., Moriarty, N. W., Oeffner, R., Read, R. J., Richardson, D. C., Richardson, J. S., Terwilliger, T. C., and Zwart, P. H. (2010) PHENIX: a comprehensive Python-based system for macromolecular structure solution. *Acta Crystallogr., Sect. D: Biol. Crystallogr. 66,* 213−221.

(38) Emsley, P., Lohkamp, B., Scott, W. G., and Cowtan, K. (2010) Features and development of Coot. *Acta Crystallogr., Sect. D: Biol. Crystallogr. 66,* 486−501.